Application of Artificial Intelligence on Magnetocardiology

Mockler-JF[1*], Yang-SH[2], Schmid-L[2], Bannasch-S[1], Maier-A[2], Park-JW[1,3]

[1]Biomagnetik Park Holding GmbH, Forsthöhe 26, 21149 Hamburg, Germany

[2]Pattern Recognition Lab, Department of Computer Science, Friedrich-Alexander-University, Martensstrasse 3, 91058, Erlangen, Germany

[3]Deutsches Herzzentrum der Charité, Campus Benjamin Franklin, Hindenburgdamm 30, Germany

*** Correspondence:**
John Mockler
john.mockler@biomagnetik.com

Keywords: Artificial Intelligence, Ischemic Heart Disease, Microcirculation, XGBoost, Magnetocardiography, Machine Learning,

Abstract

Early diagnosis and localization of the ischemic region are critical for effective treatment of ischemic heart disease (IHD), a condition which leads to a dysfunctional microcirculation in the heart. To detect the presence and extent of myocardial ischemia, functional imaging tests such as stress Positron Emission Tomography/Single Photon Emission CT Myocardial Perfusion Imaging and cardiovascular magnetic resonance are commonly used. However, they expose patients to radiation and reproducibility risks. We implement Support Vector Machines, XGBoost, Multiple Layer Perceptron Networks, and Random Forest algorithms on Magnetocardiography (MCG) data acquired from patients already confirmed to have IHD. We achieve prediction accuracies of 0.80, 0.72, and 0.70 for ischemia in the left anterior descending artery, ramus circumflexus coronary artery, and right coronary artery respectively. We further identify which MCG parameters are more useful than others and determine the best feature subset for each artery. Results show a valuable tool for early diagnosis and effective treatment of IHD.

1 Introduction

Responsible for 15.8% of all deaths, ischemic heart disease (IHD) is the leading cause of mortality worldwide [1]. It is characterized by a disturbance of the heart's microcirculation, the tiny blood vessels that supply blood directly to the heart muscle [2]. This disruption can be caused by a buildup of plaque in one or more of the larger coronary arteries that supply blood to the heart muscle. Most people with IHD do not experience any symptoms initially and are left untreated. Thus, IHD can lead to severe consequences such as myocardial infarction or sudden cardiac death. An accurate and early diagnosis is crucial for effective treatment of IHD.

Identifying myocardial ischemia in patients with suspected coronary artery disease (CAD) remains a challenging aspect of routine cardiological diagnostics. Functional or stress testing, which aims to detect inducible myocardial ischemia, has been considered the "gold standard" and is the most commonly used tool as a non-invasive method for diagnosing CAD [3]. In patients with already known chronic coronary disease (CCD) and where a change in symptoms or functional capacity is present that persists despite guideline directed management and therapy (GDMT), stress positron emission tomography/single photon emission CT myocardial perfusion imaging (PET/SPECT MPI),

cardiovascular magnetic resonance (CMR) imaging, or stress echocardiography is recommended to detect the presence and extent of myocardial ischemia, estimate risk of major adverse cardiovascular events (MACE), and guide therapeutic decision-making [4].

These non-invasive methods have been shown to have high clinical benefit but expose the patient to radiation, and are associated with significant side-effects, or have limited reproducibility. Fractional Flow Reserve (FFR) is another option for characterizing CAD. In FFR, the change in blood flow is determined by measuring the pressure drop across the obstructed coronary artery by inserting a pressure wire through guiding catheters into the ostia of coronary arteries [5]. However, FFR is invasive, and less than 40% of patients subjected to testing were found to have hemodynamically relevant obstructive CAD [6]. Caused by shortcomings of the current gold-standard diagnostic methods, there is a great need for a reliable and side-effect free method. Magnetocardiography (MCG) works by passively measuring the biomagnetic field generated by human heart cells and is therefore contactless and completely free of negative side effects. MCG has already been shown to be highly sensitive for the detection of CAD [7-10].

Abnormalities in the MCG signal during action potential, particularly during the T-wave due to an excellent signal-to-noise ratio, have been shown to be very effective in discriminating CAD [11]. An early study from Park et al. [12] showed that ischemia could be detected with a high accuracy in patients with acute chest pain, using dynamics of the positive and negative poles on the magnetic field map. Lim et al. [13] investigated the sensitivity of 24 parameters taken from the MCG signal during the QRS-complex, R-peak and T-wave for detecting non-ST-segment elevation myocardial infarction (NSTEMI). In the study, the most effective parameters for discriminating CAD were related to the angle of the vector between the negative and positive poles with the greatest magnitude on the magnetic field map, as well as the angle of the (pseudo) current vector during the T-wave, with diagnostic accuracies for individual features ranging from 62.1% to 81.4% to discriminate NSTEMI patients from age-matched controls.

Despite the limited number of labeled MCG datasets, machine learning methods for evaluating CAD have shown promise in recent years. In a study from Tao et al. [14], it was shown that MCG can reach a high degree of accuracy in the early identification of CAD using machine learning methods. Using an ensemble of SVM and XGBoost classifiers, CAD was detected with an accuracy of 0.94 with features from the time and frequency domains of the MCG signal. Furthermore, Tao et al. showed that by using the extracted time-domain features, the affected coronary artery could be identified with reasonable accuracy in patients with confirmed CAD, with an accuracy of 0.74, 0.68 and 0.65 for LAD, LCX and RCA, respectively. This performance was achieved despite extracting the parameters for the purpose of CAD detection rather than localization. The aim of this study was to reproduce and improve the results from Tao et al.

2 Materials and Methods

2.1 Materials

2.1.1 Study Population

The study was conducted retrospectively with 109 patients (92 men, 17 women, average age 79.3 +/- 12.6 years) who underwent Coronary Angiography in the Asklepios Hospital Hamburg-Harburg with the approval of the institutional review board. Written informed consent was obtained from all subjects. A positive diagnosis for CAD included at least 70% stenosis in at least one proximal epicardial coronary artery. The MCG measurements were acquired before Coronary Angiography was performed. All patients used in the study were diagnosed with CAD with stenosis in one or more

coronary arteries. Of the 109 patients, 89 were diagnosed with stenosis in the LAD artery, 55 in the LCX artery and 60 in the RCA artery. The class distributions are illustrated in Figure 1.

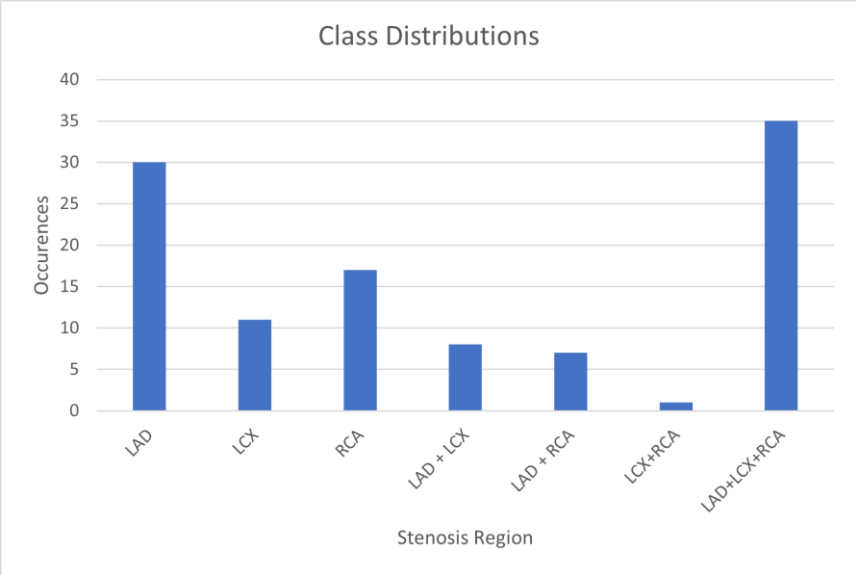

Figure 1. Class distributions with all subclasses

The measurements were acquired from a 64-channel MCG system (CS-MAG II, BMP Holding GmbH, Hamburg, Germany) [15] with a magnetically shielded room (MSR). The MCG system is equipped with superconducting quantum interference device (SQUID) first-order axial gradiometers [16, 17]. The tangential component of the magnetic field was measured at a sampling rate of 500Hz. The sensors were positioned directly above the patient's heart. The exercise MCG measurements consist of a 45 second rest phase, and a 15 second recovery (stress) phase which follows a period of exercise using a non-magnetic ergometer.

After recording, several signal processing steps were applied to prepare the data for analysis. A bandpass filter with a range of 0.3 Hz to 100 Hz was used to isolate the frequency range of interest. Additionally, a filter was employed to eliminate baseline drift. Individual heartbeats were identified in the rest and stress measurements, and each measurement was then averaged into a single, composite signal. The root-mean-square (Rms) of the averaged signals was calculated across all sensors. The QRS-complex and T-wave were then automatically identified and labeled for the rest and stress signals.

2.2 Methods

2.2.1 Feature Extraction

To train the classifiers, features which have been shown to be sensitive to identifying CAD were extracted from the overall signal. Additionally, to provide better spatial information about the location of the affected coronary artery, certain features were calculated from defined sensor clusters. Each cluster roughly represents an area of the heart which ischemia in the corresponding artery is known to affect [18]. The sensor clusters are shown in Figure 2. where the LAD cluster is located in the northern quadrant, the LCX cluster is located in the eastern quadrant, and the RCA cluster is located in the southern quadrant.

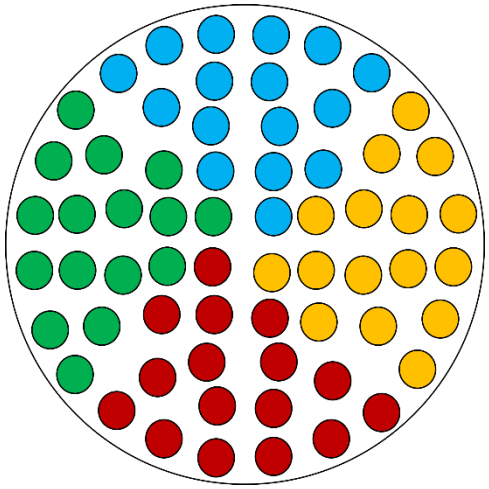

Figure 2. Sensor Configuration of Bmp MCG System. Northern sensors correspond to the LAD artery, eastern sensors correspond to the LCX artery, southern sensors correspond to the RCA artery, and western sensors are undefined

Global Features

The features described in Table 1. are based on parameters which were shown to have high diagnostic value in identifying various forms of CAD and were calculated globally across the entire sensor array. So called 'Dynamic' scores are calculated by taking the absolute difference of the local maximum and minimum of a given curve inside a sliding window.

Regional Features

The seven features described in Table 2. were extracted from the regional clusters. For each artery, a feature was calculated for both the rest and stress signal, as well as the ratio of the regional value to the value over the entire sensor array (marked as 'diff') for a total of 84 regional features.

2.2.2 Machine Learning Methods

Because of the relatively low sample-size, three binary classifiers were trained independently for the task of identifying the presence of ischemia in each respective artery rather than training a multiclass classifier on the seven subclasses. Thus, the outcome of each of the classifiers for each of the three arteries is determined and then compiled for a final result to obtain a prediction for a given sample.

To obtain the best subset of features for each classifier, an XGBoost model was first trained using the entire feature set. To determine the relative importance of each feature, the gain is calculated. In XGBoost, feature gain is a measure that helps understand how much each feature contributes to the model's ability to accurately predict outcomes, compared to other features. The best features for each artery were then selected based on empirically chosen gain thresholds, which vary for each artery.

The relatively low sample size and unbalanced class distributions could lead to problems such as overfitting or outliers having a large effect on the trained model. To attempt to balance the dataset, manifold learning was applied to divide the data, which has shown to be more effective than random division [19]. In manifold-based learning, the data is projected into a lower-dimensional space (in this case, 3-dimensions), while attempting to retain distances between local neighbors. The data is then clustered into new classes and the training and test set are formed by randomly sampling the re-labeled data while maintaining the proportions of the newly clustered classes.

To generate the results, five-fold cross validation was used. Within each round of cross validation, four different classifiers were independently trained on the feature subset - XGBoost, Linear Support Vector Machine (SVM), Multilayer Perceptron (MLP) and Random Forest (RF). The results of the three best performing classifiers were then averaged together with equal weights as an ensemble for the final prediction.

To reduce overfitting and further address the class imbalance problem, the minority class in each training set was augmented using Synthetic Minority Oversampling Technique (SMOTE) [20]. For a binary classification problem, SMOTE attempts to augment the minority class by creating synthetic samples. Each synthetic sample is generated by randomly selecting a sample from the minority class, identifying its five nearest neighbors, randomly selecting a nearest neighbor and creating a synthetic sample at a random distance between the selected sample and its selected neighbor. The machine learning workflow is depicted in Figure 3.

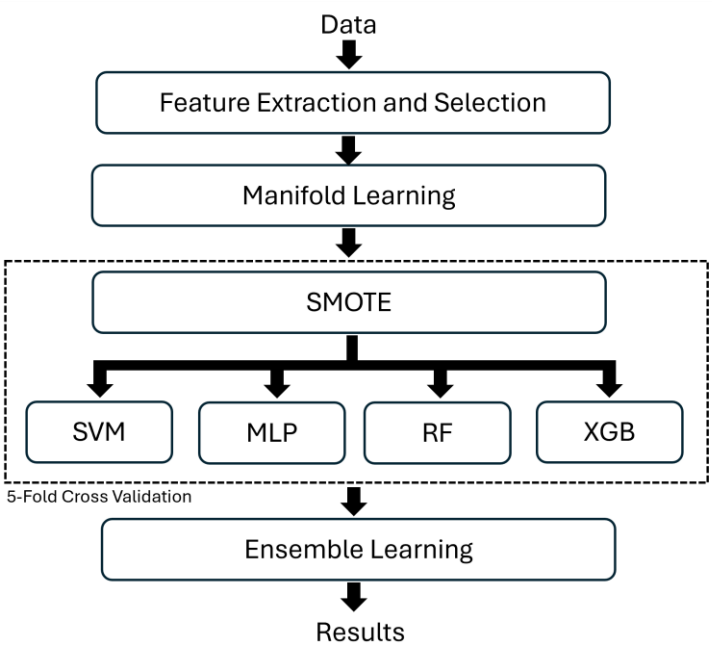

Figure 3. Machine learning workflow

2.2.3 Scoring Methods

The following scoring methods were used to evaluate the model: accuracy, precision, recall, F1 score, Receiver Operating Characteristic (ROC) curve, and Precision-Recall Curve. F1 score is defined as the harmonic mean of precision and recall, and is calculated in the following equation,

$$F1 = \frac{TP}{TP + \frac{1}{2}(FP + FN)}$$

Where TP is the number of true positive classifications, FP is the number of false positive classifications, and FN is the number of false negative classifications.

3 Results

The issue of identifying the stenosis location was separated into three binary classifications, predicting whether a stenosis was present in each of the three arteries. The best feature subgroups were identified for each stenosis location, and four classifiers were trained using these feature sets, with the top three models forming an ensemble average classifier.

The classifier was trained using parameters extracted solely from the rest signal, solely from the stress signal, and from both the rest and stress signals. By utilizing rest-only features, we obtained accuracies of 0.79, 0.68, and 0.67 for LAD, LCX, and RCA, respectively. Similarly, with stress-only features, we achieved accuracies of 0.78, 0.69, and 0.60 for LAD, LCX, and RCA. By combining both rest and stress features, we attained accuracies of 0.80, 0.72, and 0.70 for LAD, LCX, and RCA. Due to the random nature of data splitting, this process was repeated ten times for each feature set, and the results were averaged to account for any variations. The results are shown with standard deviations in Tables 3-5.

For the LAD artery, the classifier trained on both rest and stress features achieved an accuracy of 0.80, with a precision of 0.86, recall of 0.86, and an F1 score of 0.86. The ten best features, ranked by the feature importance weight from XGBoost, are displayed in Figure 4. The ROC and Precision-Recall area under the curve values were 0.798 and 0.922 respectively.

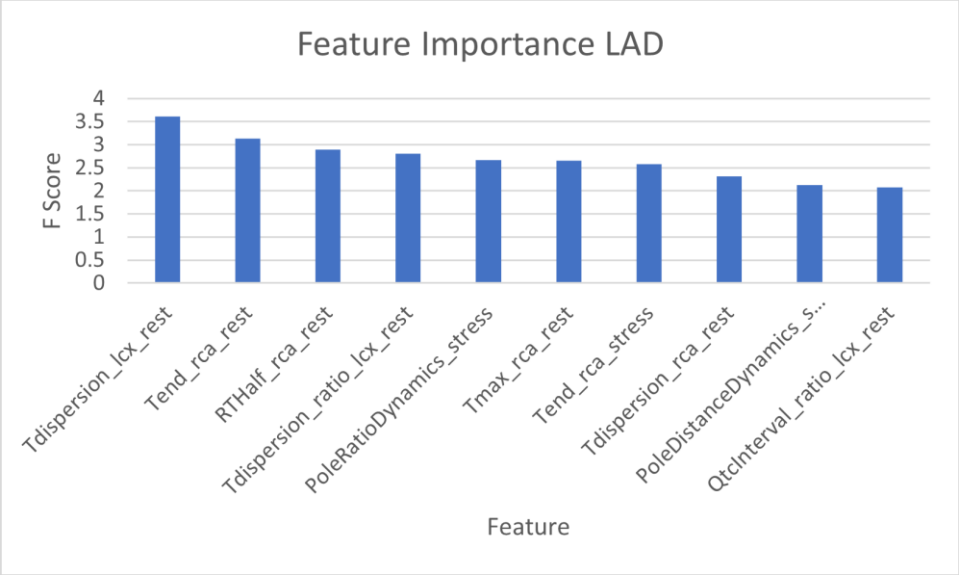

Figure 4. Feature importances for LAD artery

The prediction distribution for LAD is shown in Figure 5. The predictor performed best for LAD only patients and patients with multiple affected arteries, while performing relatively poorly for RCA and LCX, with LCX having an accuracy of 0.55.

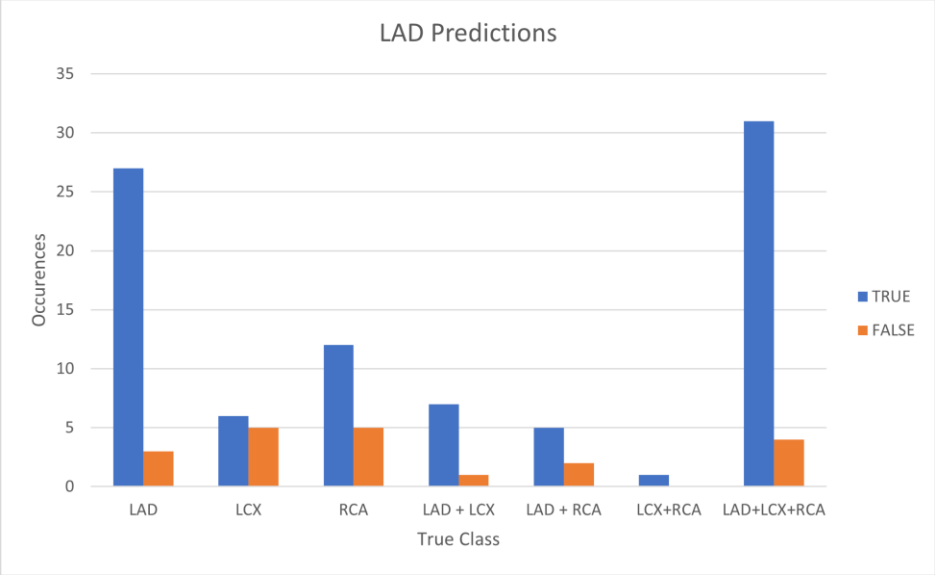

Figure 5. Predictions for each subclass for LAD artery

For the LCX artery, the classifier trained on both rest and stress features achieved an accuracy of 0.72, with a precision of 0.72, recall of 0.73, and an F1 score of 0.72. The ten best features, ranked by the feature importance weight from XGBoost, are displayed in Figure 6. The ROC and Precision-Recall area under the curve values were 0.77 and 0.79 respectively.

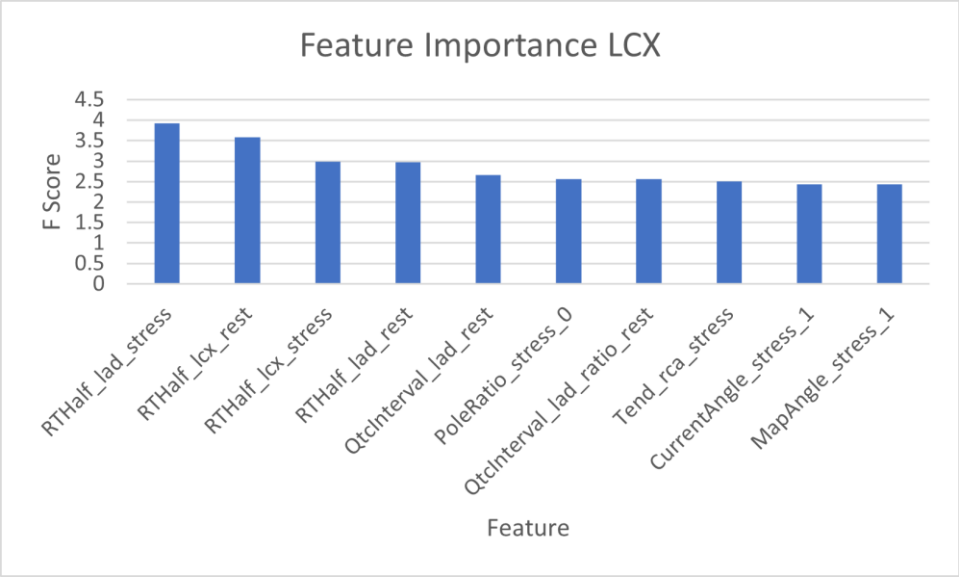

Figure 6. Feature importances for LCX artery

The prediction distribution for LCX is shown in Figure 7. The predictor performed best for RCA and LAD+LCX patients. The worst class to predict LCX (or absence thereof) was LAD+RCA, with a prediction accuracy of 0.57.

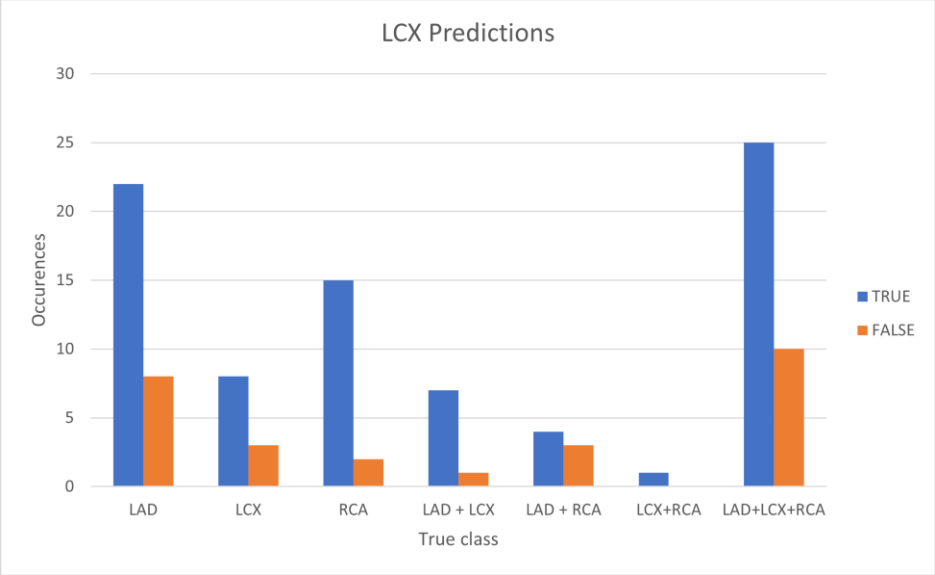

Figure 7. Predictions for each subclass for LCX artery

For the RCA artery, the classifier trained on both rest and stress features achieved an accuracy of 0.70, with a precision of 0.73, recall of 0.73, and an F1 score of 0.73. The ten best features, ranked by the feature importance weight from XGBoost, are displayed in Figure 8. The ROC and Precision-Recall area under the curve values were 0.67 and 0.76 respectively.

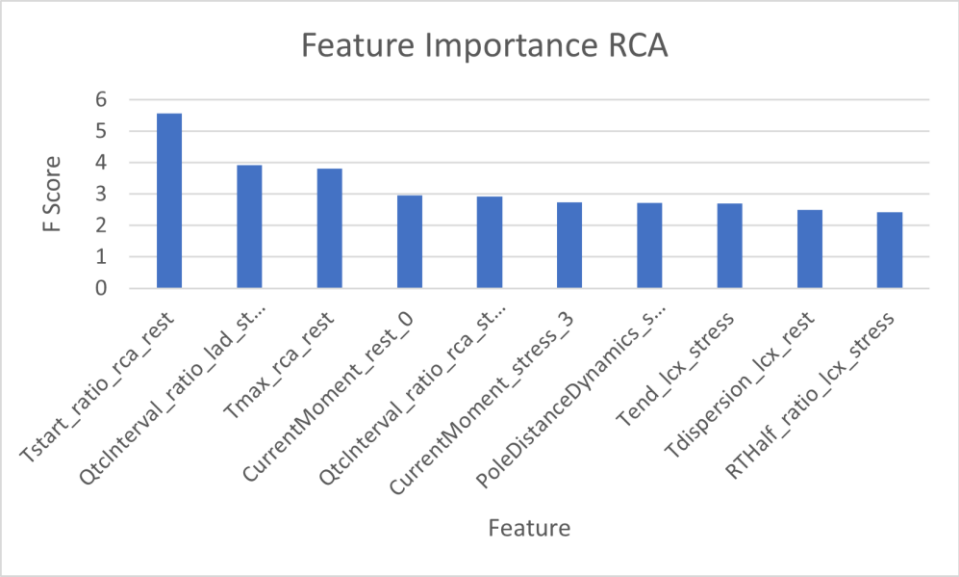

Figure 8. Feature importances for RCA artery

The prediction distribution for RCA is shown in Figure 9. The only class prediction with high accuracy was for patients with all three affected arteries. Notably, the classifier only correctly predicted LCX patients with an accuracy of 0.36.

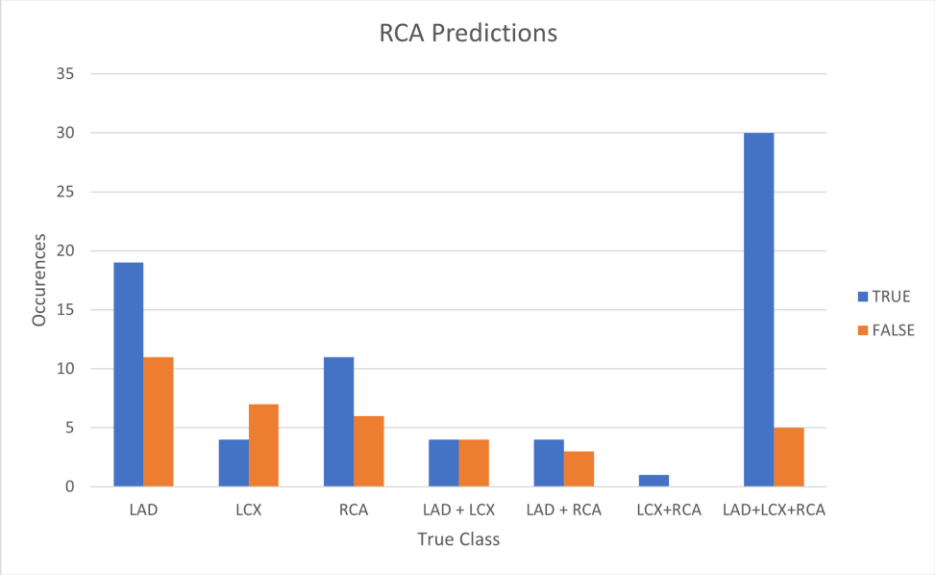

Figure 9. Predictions for each subclass for LCX artery

4 Discussion

In this study, we developed a machine learning classifier for the task of localizing stenoses in patients with CAD. Combining the results of the three best classifiers as an ensemble average, we achieved accuracies of 0.79, 0.68, and 0.67 for LAD, LCX, and RCA, respectively, using only the rest features. By considering only the stress features, the accuracies were to 0.78, 0.69, and 0.60 for LAD, LCX, and RCA, respectively. By utilizing both rest and stress features, the accuracies reached 0.80, 0.72, and 0.70 for LAD, LCX, and RCA.

It is important to note that since the sampled patients presented with acute chest pain, the majority of them likely already had significant ischemia at rest. This may explain why the addition of stress features only resulted in moderate improvements of the measured values. However, the relatively smaller subset of patients with moderate or no ischemia at rest, but induced ischemia under stress, could account for the observed small improvement in results. The results align with the findings of Tao et al. [14], who achieved prediction accuracies of 0.74, 0.68, and 0.65 for LAD, LCX, and RCA, respectively, using only rest measurements. However, direct comparison is challenging due to the inherent noise differences between unshielded MCG systems such as the ones used in Tao. et al. and shielded MCG systems such as the one used in this study. Unshielded MCG signals inherently contain more noise, and noise reduction techniques such as higher order gradiometers can remove information from the signal, making it difficult to evaluate our findings against Tao et al. as a diagnostic tool for localizing CAD without knowledge of the exclusion criteria used in both studies [21].

Tao et al. [14] used features extracted from the time domain, frequency domain and features based on information theory, using the same feature set for both detection and localization of IHD. Similarly, we used features from the time domain, which have been shown in previous studies to be sensitive in predicting IHD in patients. To further improve upon localization results, we hypothesized that by extracting features from regions aligned with the areas affected by stenosis in each coronary artery, it would allow the classifier to better distinguish between stenoses located in them. This sensor clustering approach proved valuable in predicting each class, with regional features comprising eight of ten of the highest weighted features for LAD and seven of ten for both LCX and

RCA. However, there seemed to be weak correlation with the region of stenosis and the sensor cluster where the more sensitive features were extracted from. This leads to the conclusion that dividing the sensor array into regions and calculating the parameters on these regions can be helpful in differentiating stenosis in the arteries by providing spatial information of the heart signal, but a stenosis does not necessarily lead to significant changes in its aligned cluster. This suggests that creating more, smaller sensor clusters could also prove to be useful in localizing ischemia. Besides the regional clusters, the only global scores included in the top feature importances were pole ratio and distance dynamics for LAD, pole ratio, current angle and map angle for LCX and current moment for RCA, all of which provide information about the direction and strength of electric activity in the heart.

Interestingly, despite the RCA and LCX patients having a similar number of occurrences and the RCA artery being the only afflicted artery in more cases, both the paper from Tao et al. [14] and this study consistently observed a higher prediction rate of stenosis in the LCX artery by the classifier. Particularly, the classifier showed significantly higher relative prediction rates in patients with three afflicted arteries, which could indicate that the positive prediction is based on the relative severity of the disease. The classifier's performance notably declined in cases with a single afflicted artery, where a majority (63.4%) of LCX patients were incorrectly predicted to have stenosis in the RCA artery. This suggests potential overlap in the features indicative of stenosis between the RCA and LCX arteries, emphasizing the importance of identifying more distinctive features specific to the RCA artery, i.e., extracting parameters from more granular sensor clusters. This further emphasizes the importance of feature identification in localization. In fact, the selection of features to include in each model also significantly influenced the results. Therefore, future work would be in identifying more descriptive features which provide more unique MCG signal changes for each artery, as well as optimizing the feature selection process, applying more advanced feature selection and elimination methods.

Despite the promising results, there are clear limitations in the study. With only 109 subjects, the data set was still relatively small with significant class imbalances, restricting the generalizability of the findings. While data augmentation techniques helped address these imbalances, it is crucial to verify and improve the model with a larger, more balanced data set. Future research should focus on investigating the relationship between the subclasses, and their impact on the cardiovascular system. We envision that this will improve the generalizability and consolidate our model findings.

4.1 Outlook

Our study presents a machine learning classifier for localizing stenoses in patients with CAD using magnetocardiography. The achieved accuracies, which surpass those of a previous study, highlight the potential of this non-invasive technique for both early detection and localization of stenoses. The study introduced a clustering approach to extract features from specific regions, aiming to improve the classifier's ability to distinguish between stenoses in each artery. However, there was a weak correlation between the region of stenosis and the cluster from which sensitive features were extracted. This suggests that dividing the sensor array into more, smaller clusters could be beneficial in localizing ischemia. Future works will include improving the current classification result across multiple arteries by using more balanced class database. Moreover, acquiring larger dataset will enable us to compare with neural network algorithms.

5 Conflict of Interest

Jai-Wun Park owns stock in Biomagnetik Park Holding GmbH, a company developing MCG systems targeting diagnoses of heart diseases and has patents on MCG systems. John F. Mockler, and Sebastian Bannasch, are employees of Biomagnetik Park Holding GmbH.

6 Author Contributions

JFM and LS conducted the experiments and evaluations. SHY and JFM conducted the writing of the article and the interpretation and discussion of results. SHY, SB, AM, and JWP did the conceptual design of the work and supervised the research.

7 Funding

We acknowledge financial support by Deutsche Forschungsgemeinschaft and Friedrich-Alexander-Universität Erlangen-Nürnberg within the funding programme “Open Access Publication Funding”.

8 Acknowledgement

JFM and LS conducted the experiments and evaluations. SHY and JFM conducted the writing of the article and the interpretation and discussion of results. SHY, SB, AM, and JWP did the conceptual design of the work and supervised the research.

9 References

[1] Institute of Medicine (US) Committee on Social Security Cardiovascular Disability Criteria. Cardiovascular Disability: Updating the Social Security Listings. Washington (DC): National Academies Press (US); 2010. 7, Ischemic Heart Disease. Available from: https://www.ncbi.nlm.nih.gov/books/NBK209964/

[2] Matschke K, Jung F. Regulation of the myocardial microcirculation. Clin Hemorheol Microcirc. 2008;39(1-4):265-79.

[3] Levine GN, Bates ER, Bittl JA, Brindis RG, Fihn SD, Fleisher LA, Granger CB, Lange RA, Mack MJ, Mauri L, Mehran R. 2016 ACC/AHA guideline focused update on duration of dual antiplatelet therapy in patients with coronary artery disease: a report of the American College of Cardiology/American Heart Association Task Force on Clinical Practice Guidelines: an update of the 2011 ACCF/AHA/SCAI guideline for percutaneous coronary intervention, 2011 ACCF/AHA guideline for coronary artery bypass graft surgery, 2012 ACC/AHA/ACP/AATS/PCNA/SCAI/STS guideline for the diagnosis and management of patients with stable ischemic heart .... Circulation. 2016 Sep 6;134(10):e123-55.

[4] Writing Committee Members, Virani SS, Newby LK, Arnold SV, Bittner V, Brewer LC, Demeter SH, Dixon DL, Fearon WF, Hess B, Johnson HM. 2023 AHA/ACC/ACCP/ASPC/NLA/PCNA guideline for the management of patients with chronic coronary disease: a report of the American Heart Association/American College of Cardiology Joint Committee on Clinical Practice Guidelines. Journal of the American College of Cardiology. 2023 Aug 29;82(9):833-955.

[5] Pijls NH, de Bruyne B, Peels K, van der Voort PH, Bonnier HJ, Bartunek J, Koolen JJ. Measurement of fractional flow reserve to assess the functional severity of coronary-artery stenoses. New England Journal of Medicine. 1996 Jun 27;334(26):1703-8.

[6] Patel MR, Peterson ED, Dai D, Brennan JM, Redberg RF, Anderson HV, Brindis RG, Douglas PS. Low diagnostic yield of elective coronary angiography. New England Journal of Medicine. 2010 Mar 11;362(10):886-95.

[7] Shin ES, Lam YY, Her AY, Brachmann J, Jung F, Park JW. Incremental diagnostic value of combined quantitative and qualitative parameters of magnetocardiography to detect coronary artery disease. International journal of cardiology. 2017 Feb 1;228:948-52.

[8] Park J.-W, Hill PM, Chung N, Hugenholtz PG, Jung F. Magnetocardiography predicts coronary artery disease in patients with acute chest pain. Ann Noninvasive Electrocardiol 2005; 10: 312 - 323.

[9] J.-W. Park, B. Leithäuser, M. Vršansky, F. Jung. Dobutamine stress magnetocardiography for the detection of significant coronary artery stenoses – A prospective study in comparison with simultaneous 12-lead electrocardiography. Clin Hemorheol Microcirc 39; 21 – 32: 2008.

[10] Park JW, Shin ES, Ann SH, Gödde M, Park LS, Brachmann J, Vidal-Lopez S, Wierzbinski J, Lam YY, Jung F. Validation of magnetocardiography versus fractional flow reserve for detection of coronary artery disease. Clin Hemorheol Microcirc 59 (2014), 267 – 281.

[11] Camm AJ, Henderson R, Brisinda D, Body R, Charles RG, Varcoe B, Fenici R. Clinical utility of magnetocardiography in cardiology for the detection of myocardial ischemia. J Electrocardiol; 2019 Nov-Dec;57:10-17. doi: 10.1016/j.jelectrocard.2019.07.009. Epub 2019 Jul 25. PMID: 31442563.

[12] Park JW, Hill PM, Chung N, Hugenholtz PG, Jung F. Magnetocardiography predicts coronary artery disease in patients with acute chest pain. Ann Noninvasive Electrocardiol. 2005 Jul;10(3):312-23. doi: 10.1111/j.1542-474X.2005.00634.x. PMID: 16029382; PMCID: PMC6932599.

[13] Lim HK, Chung N, Kim K, Ko YG, Kwon H, Lee YH, Kim JM, Joung B, Kim JB, Yu KK, Cho JR. Can magnetocardiography detect patients with non-ST-segment elevation myocardial infarction?. Annals of medicine. 2007 Jan 1;39(8):617-27.

[14] Tao R, Zhang S, Huang X, Tao M, Ma J, Ma S, Zhang C, Zhang T, Tang F, Lu J, Shen C. Magnetocardiography-based ischemic heart disease detection and localization using machine learning methods. IEEE Transactions on Biomedical Engineering. 2018 Oct 23;66(6):1658-67.

[15] Lee YH, Yu KK, Kim JM, Kwon H, Kim K. A high-sensitivity magnetocardiography system with a divided gradiometer array inside a low boil-off Dewar. Superconductor Science and technology. 2009 Oct 20;22(11):114003.

[16] YH L. Double relaxation oscillation SQUID with high flux-to-voltage transfer and its application to a biomagnetic multichannel system. J Korean Phys Soc. 1998;32:600-5.

[17] Kim K. Correction in the principal component elimination method for neuromagnetic evoked field measurements. J. Kor. Phys. Soc.. 2004;44:980-6.

[18] Bayes de Luna A. New heart wall terminology and new electrocardiographic classification of Q-wave myocardial infarction based on correlations with magnetic resonance imaging. Revista espanola de cardiologia. 2007 Jul 1;60(7):683-9.

[19] Chen S, Dorn S, Lell M, Kachelrieß M, Maier A. Manifold learning-based data sampling for model training. In Bildverarbeitung für die Medizin 2018: Algorithmen-Systeme-Anwendungen. Proceedings des Workshops vom 11. bis 13. März 2018 in Erlangen 2018 (pp. 269-274). Springer Berlin Heidelberg.

[20] Chawla NV, Bowyer KW, Hall LO, Kegelmeyer WP. SMOTE: synthetic minority over-sampling technique. Journal of artificial intelligence research. 2002 Jun 1;16:321-57.

[21] Koch H. SQUID magnetocardiography: Status and perspectives. IEEE transactions on applied superconductivity. 2001 Mar;11(1):49-59. doi:10.1109/77.919284

10 Tables

10.1 Table 1, Global Parameter descriptions

Parameter	**Description**
Monopolarity Curve Average Slope (Tbegin to Tend)	The monopolarity curve is calculated using the equation, $m_t = \frac{\left\lvert\sum_i^n b_{i,t}\right\rvert}{\sum_i^n \left\lvert b_{i,t}\right\rvert}$, Where m_t is the degree of monopolarity at sample t, n is the number of sensors, and $b_{i,t}$ is the magnetic field value measured at sensor i at sample t. The average slope of the monopolarity curve is then calculated between T-begin and T-max. [Erhlen16]
T-wave Dispersion	Deviation of the time point of T-max across all sensors.
Current Moment (on 8 evenly distributed time steps between Tbegin and Tend)	The magnitude of the pseudo current moment vector.

Current Moment Dynamics (on 8 evenly distributed time steps between Tbegin and Tend)	The dynamics of the magnitude of the pseudo current moment vector.
Current Angle (on 8 evenly distributed time steps between Tbegin and Tend)	The angle of the pseudo current moment vector.
Current Angle Dynamics (on 8 evenly distributed time steps between Tbegin and Tend)	The dynamics of the angle of the pseudo current moment vector.
Field Map Angle (on 8 evenly distributed time steps between Tbegin and Tend)	The field map angle, defined as the angle of the vector going from the minimum to maximum value on the magnetic field map.
Pole Distance (on 8 evenly distributed time steps between Tbegin and Tend)	The distance in milimeters between the minimum to maximum values on the magnetic field map.
Pole Ratio (on 8 evenly distributed time steps between Tbegin and Tend)	The ratio of the maximum to minimum value on the magnetic field map.
ST_T Angle Dynamics Score	1 when the current angle dynamics are pathologic, 0 otherwise.
ST_T Distance Dynamics Score	1 when the pole distance dynamics are pathologic, 0 otherwise.
ST_T Ratio Dynamics Score	1 when the pole ratio dynamics are pathologic, 0 otherwise.
VMCG Score	1 when the distance between the magnetic dipole moment vector at T start and T end is pathologic, 0 otherwise.

Monopolarity Curve Average Slope Subscore	1 when the monopolarity curve slope is positive, 0 otherwise.
TWave Dispersion Score	When the T-wave dispersion is greater than an upper threshold, a score of 2 is given, if the dispersion is greater than a middle threshold, a score of 1 is given, 0 otherwise.

10.2 Table 2, Regional parameter descriptions

Parameter	**Description**
T Dispersion	The RMS-averaged distance from the mean T-wave.
QTc	The mean QTc interval time.
QRSMax	The average *Rmax* magnitude, normalized by the RMS *Rmax.*
Halfway between Rmax and Tmax (RT-Half)	The average magnitude of the halfway point between *Rmax* and Tmax, normalized by the RMS *Rmax.*
TStart	The average TStart magnitude, normalized by the RMS *Rmax.*
TMax	The average TMax magnitude, normalized by the RMS *Rmax.*
TEnd	The average TEnd magnitude, normalized by the RMS *Rmax.*

10.3 Table 3, Results with only rest parameters

Class	Accuracy	Precision	Recall	F1
LAD	0.79 ± 0.016	0.86 ± 0.006	0.84 ± 0.020	0.85 ± 0.012
LCX	0.68 ± 0.017	0.68 ± 0.029	0.72 ± 0.041	0.70 ± 0.015
RCA	0.67± 0.022	0.68 ± 0.028	0.76 ± 0.024	0.71 ± 0.008

10.4 Table 4, Results with only stress parameters

Class	Accuracy	Precision	Recall	F1
LAD	0.78 ± 0.006	0.88 ± 0.004	0.82 ± 0.008	0.85 ± 0.005
LCX	0.69 ± 0.012	0.69 ± 0.008	0.73 ± 0.035	0.71 ± 0.018
RCA	0.60 ± 0.008	0.62 ± 0.005	0.71 ± 0.038	0.66 ± 0.016

10.5 Table 5, Results with rest and stress parameters combined

Class	Accuracy	Precision	Recall	F1
LAD	0.80 ± 0.014	0.86 ± 0.002	0.86 ± 0.014	0.86 ± 0.010
LCX	0.72 ± 0.010	0.72 ± 0.010	0.73 ± 0.017	0.72 ± 0.011
RCA	0.70 ± 0.011	0.73± 0.009	0.73 ± 0.017	0.73 ± 0.012